ACS APPLIED POLYMER MATERIALS

pubs.acs.org/acsapm

Article

Silk Fibroin Cryogel Building Adaptive Organohydrogels with Switching Mechanics and Viscoelasticity

Berkant Yetiskin and Oguz Okay*

Cite This: *ACS Appl. Polym. Mater.* 2022, 4, 5234−5245

Read Online

ACCESS | Metrics & More | Article Recommendations | Supporting Information

ABSTRACT: In contrast to synthetic gels, their biological counterparts such as cells and tissues have synergistic biphasic components containing both hydrophilic and lyophilic phases, providing them some special abilities including adaptive biomechanics and freezing tolerance. Hydrogels containing both hydrophilic and lyophilic phases, referred to as organohydrogels (OHGs), are capable of mimicking the biological systems, and they might have great potential in various applications. Here, we present a facile strategy to obtain adaptive OHGs with tunable and programmable mechanics and viscoelasticity. We utilize a hydrophilic cryogel scaffold as the continuous phase of OHGs, while the pores of the scaffold act as the reaction loci for the formation of organogel microinclusions. Thus, we first prepared mechanically robust cryogels based on silk fibroin (SF) via cryogelation reactions at −18 °C. The cryogels with 94% porosity containing interconnected μm-sized pores were then immersed in an ethanolic solution of acrylic acid (AAc), *n*-octadecyl acrylate (C18A), *N*,*N*′-methylenebis(acrylamide), and a free-radical initiator. Polymerization reactions conducted within the pores of the cryogels lead to mechanically strong adaptive OHGs consisting of a SF scaffold containing semi-crystalline poly(AAc-*co*-C18A) organogel microinclusions. The mechanical strength of OHGs is much higher than that of their components due to the significant energy dissipation in the OHG networks. Depending on the amount of the crystallizable C18A monomer units, the melting temperature T_m and the degree of crystallinity of OHGs could be varied between 49 and 54 °C and 1.3 and13%, respectively. The crystallinity created in OHGs provided them switchable mechanics and viscoelasticity in response to a temperature change between below and above T_m. All OHGs exhibited shape-memory function with a shape-recovery ratio of more than 92%. The strategy developed here to obtain high-strength smart OHGs is suitable for a wide variety of combinations of hydrophilic scaffolds and organogels.

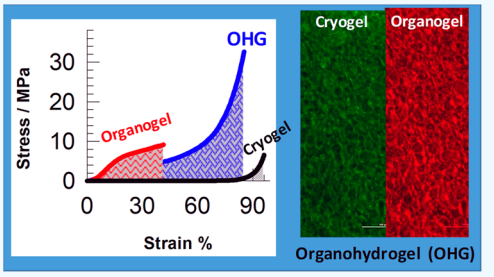

KEYWORDS: *organohydrogels, cryogels, silk fibroin, n-octadecyl acrylate, shape memory*

Downloaded via ISTANBUL TEKNIK UNIV on July 15, 2022 at 15:15:27 (UTC).
See https://pubs.acs.org/sharingguidelines for options on how to legitimately share published articles.

1. INTRODUCTION

In contrast to synthetic gels, their biological counterparts such as cells and tissues have synergistic biphasic components containing both hydrophilic and lyophilic phases simultaneously, which showed up during billions of years by evolutionary natural selection.[1] Such coexistence of the antagonistic features in the body provides some special abilities including adaptive biomechanics and freezing tolerance. For instance, echinoderms such as sea cucumber and starfish possessing mutable collagenous tissue, which enables a nervous system-induced stiffness altering, can regulate their body mechanics as soft and hard modes, when they are at rest and threatened, respectively.[2−4] Moreover, arctic wood frogs containing specialized proteins called antifreeze proteins, which possess both hydrophilic and lyophilic fragments, can live in harsh and cold environments without freezing.[5,6] These evolutionary adaptations of the biological systems have always been a model for scientists to develop new-generation synthetic smart materials. Such materials containing both hydrophilic and lyophilic phases can be referred to as OHGs, and they might have great potential in various applications including sensors of humidity,[7] strain,[8−11] and temperature,[12] microfluidic and optical devices,[13,14] signal transmission,[15] freeze-tolerant materials,[16−18] and soft robotics.[19]

One generally used strategy to prepare an OHG is dispersing a discontinuous organic (lyophilic) phase in a continuous aqueous phase to obtain an oil-in-water emulsion.[4,20] These kinds of systems are thermodynamically unstable emulsion systems, and their kinetic stabilization needs some special stabilizers such as amphiphilic copolymers, nanoparticles, or surfactants.[19,21,22] Recently, OHGs prepared in the absence of a stabilizer were also reported, in which bi-step manufacturing techniques were used. For instance, Gao et al. synthesized freeze-tolerant OHGs after UV irradiation of a system formed via the infusion of a lyophilic phase to a pre-synthesized and

Received: May 2, 2022
Accepted: June 13, 2022
Published: June 23, 2022

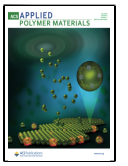

© 2022 The Authors. Published by American Chemical Society

Scheme 1. Cartoon Presenting Formation of OHGs[a]

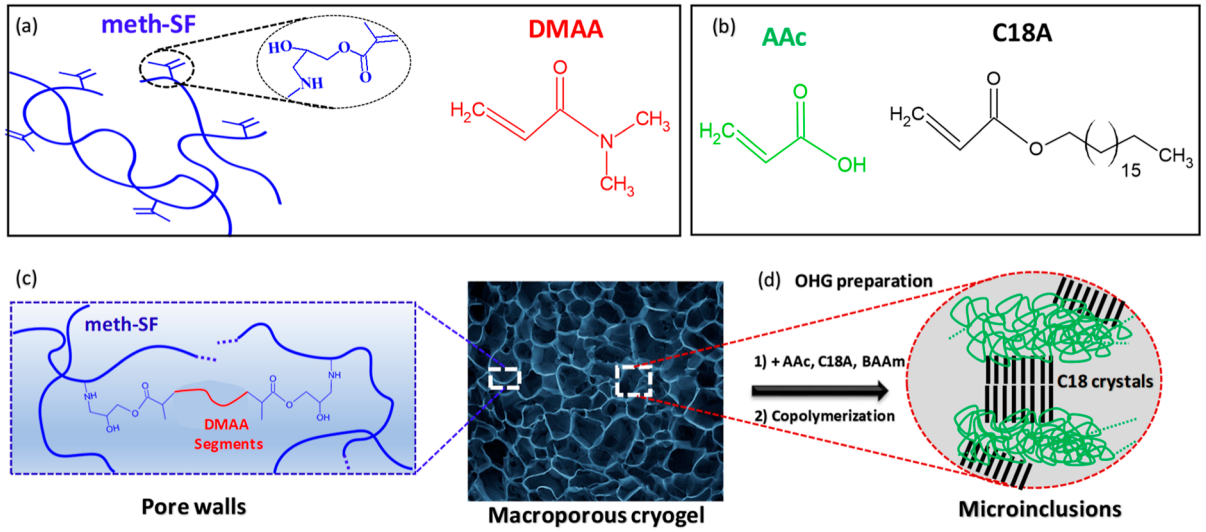

[a](a,b) Components of the aqueous cryogel (a) and organic phases (b) of the OHG. (c) Chemical composition of the pore walls of the cryogel scaffold. (d) Formation of OHG via filling of the pores of the cryogel with AAc, C18A, and BAAm monomers, followed by copolymerization, in the presence of AIBN to produce microinclusions with semicrystalline poly(AAc-*co*-C18A) organogel.

dehydrated poly(*N*,*N*-dimethylacrylamide) gel network.[23] In a similar manner, anti-freezing compounds including glycerol, glycol, and sorbitol were introduced into a pre-obtained Ca-alginate/poly(acrylamide) gel network in order to fabricate non-freezable materials.[17] However, these kinds of studies are mainly focused on the freeze-tolerant properties of the materials rather than the switchable mechanical and viscoelastic abilities. In addition, the first network of these OHGs is classical hydrogels possessing insufficient mechanical properties due to poor energy dissipation.[24,25]

Here, we present a facile strategy to obtain adaptive OHGs with tunable and programmable mechanics and viscoelasticity. Instead of dispersing the lyophilic phase in a continuous aqueous phase, we utilize a macroporous hydrophilic cryogel scaffold as the continuous phase, while the pores of the scaffold act as the reaction loci for the formation of microinclusions, as schematically illustrated in Scheme 1.

Cryogelation, that is, gelation conducted below the freezing point of the reaction system is a very efficient method for the preparation of tough macroporous materials having an interconnected open porous architecture.[26−30] In contrast to the classical hydrogels, the cryogels possess permanent pores independent of the drying conditions, and exhibit extraordinary mechanical properties such as superior compressibility (>95%) and fatigue resistance in addition to rapid water absorption/desorption capability occurred within seconds.[29,31−39] These abilities provide them an advantage over the traditional hydrogels, especially for load bearing applications.

In the present study, we first prepared mechanically robust cryogels based on methacrylated silk fibroin (SF) and *N*,*N*-dimethylacrylamide (DMAA) as a spacer via cryogelation reactions at −18 °C (Scheme 1a,c). The cryogels with 94% porosity containing interconnected μm-sized pores were then immersed in an ethanolic solution of the hydrophilic acrylic acid (AAc) monomer, crystallizable hydrophobic *n*-octadecyl acrylate (C18A) comonomer, *N*,*N*′-methylenebis(acrylamide) (BAAm) cross-linker, and a free-radical initiator (Scheme 1b). As typical for many cryogels,[29] SF cryogels do not swell in this solution by volume, but their mass significantly increases due to the filling of their pores with the solution. Free-radical polymerization reactions conducted within the pores of the cryogels lead to mechanically strong adaptive OHGs consisting of a SF scaffold containing semi-crystalline poly(AAc-*co*-C18A) organogel microinclusions (Scheme 1c,d). As will be seen below, the mechanical strength of OHGs is much higher than that of their components due to the significant energy dissipation in the OHG networks. The melting temperature, T_m, and the degree of crystallinity of OHGs could be varied between 49 and 54 °C and 1.3 and13%, respectively, by varying the amount of the crystallizable C18A units in the organogel component. The crystallinity created in OHGs provided them switchable mechanics and viscoelasticity in response to a temperature change between below and above T_m. What is more, all OHGs exhibited shape-memory function with a shape-recovery ratio of more than 92%.

2. RESULTS AND DISCUSSION

In the following, we first discuss the preparation and characteristics of SF cryogels forming the continuous phase of the OHGs. The copolymerization of AAc and C18A monomers within the macropores of the cryogels and the properties of OHGs containing organogel microinclusions are then discussed in the following sections.

2.1. SF Cryogel Scaffold of OHGs. A SF-based cryogel scaffold used as the skeleton of OHGs was prepared from an aqueous solution of methacrylated SF (meth-SF) with a methacrylation degree of 14% and DMAA monomer as a spacer (Scheme 1a). 1,4-Butanediol diglycidyl ether (BDDE) was the cross-linker for SF, while the ammonium persulfate (APS) and *N*,*N*,*N*′,*N*′-tetramethylethylenediamine (TEMED) redox system was the initiator for DMAA. The synthesis conditions were the same as those of the SF hydrogels we reported before,[40] except that the reaction temperature was reduced from 50 to −18 °C to provide cryogenic conditions. In the preliminary experiments, the concentrations of meth-SF and DMAA were varied over a wide range to optimize the cryogel properties suitable for OHG preparation, that is, the

https://doi.org/10.1021/acsapm.2c00741
ACS Appl. Polym. Mater. 2022, 4, 5234−5245

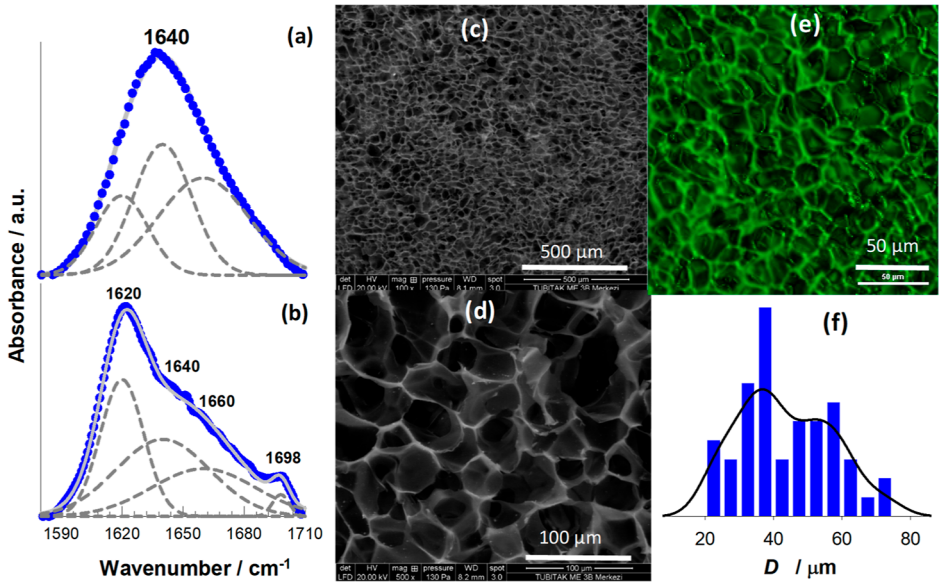

Figure 1. (a,b) FTIR spectra of meth-SF before (a) and after (b) cryogelation. The blue symbols represent the original data, while the solid and dashed curves represent the fitted spectra and hidden peaks, respectively. (c−e) SEM (c,d) and confocal microscopy (e) images of SF scaffolds. The sample in (e) was stained green using the fluorescein isothiocyanate isomer I (FITC). (f) Size distribution of the pores in the scaffold.

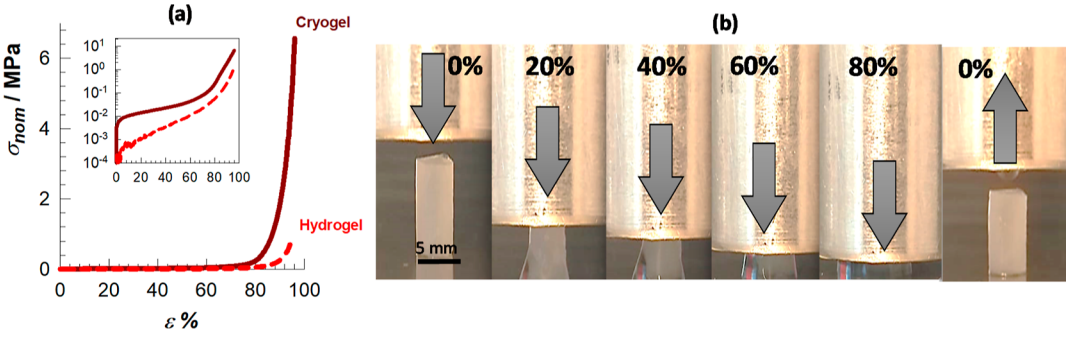

Figure 2. (a) Nominal stress (σ_{nom})−strain (ε) curves of the wet cryogel and hydrogel formed at −18 and 50 °C, respectively. The inset represents a semi-logarithmic plot of the same data. (b) Images of a wet cryogel specimen during compression to 80% strain followed by unloading to zero strain.

highest weight swelling ratio, porosity and gel fraction, and the largest pore size, together with good mechanical properties (Figures S1−S3). The cryogel scaffold with the optimum properties could be obtained from an aqueous solution of 5 w/v % meth-SF and 2 w/v % DMAA, that is, the pore walls of the cryogel are composed of 71 wt % SF and the rest is poly(DMAA) (PDMAA) which is a biocompatible polymer (Scheme 1c).[41−43] The extraction tests in water revealed that the gel fraction W_g is 0.84 ± 0.02, indicating that 84% of SF and PDMAA are incorporated into the cross-linked cryogel network (Figure S1). The conformation analysis of SF of the cryogel could not be conducted by both Fourier transform infrared (FTIR) and X-ray diffraction (XRD) techniques due to the overlapping peaks of PDMAA and SF.[40] Therefore, we carried out FTIR measurements on the cryogel prepared under the same experimental conditions but in the absence of DMAA. Figure 1a,b shows FTIR spectra of meth-SF before (a) and after (b) cryogelation. The symbols represent the original data, while the solid and dashed curves represent the fitted spectra and hidden peaks at 1620, 1640, 1660, and 1698 cm^{-1} due to the β-sheets, random coil, α-helix, and β-turn configurations, respectively.[44−46] Calculations reveal that the content of β-sheets increases from 15 to 32% after cryogelation reactions, which is responsible for the formation of a water-insoluble scaffold (Figure S4). We should note that the β-sheet content of the present SF cryogels is lower than that of the corresponding SF hydrogels formed at 50 °C.[40,46] This is due to the decreasing reaction temperature impeding conformation transition in fibroin. However, when compared with the cryogels based on native SF,[34] they exhibit a similar β-sheet content (33 ± 2%).

The weight (q_w) and volume swelling ratios (q_v) of the cryogel in water were determined as 13 ± 1 and 1.0 ± 0.1, respectively (Figure S1). Thus, there is no volume change of the cryogel when immersed in water, while its mass increases 13-fold, indicating that the gel swelling is due to the filling of the pores by water. In the following, we will use the term "wet cryogel" instead of "swollen cryogel" as no swelling of the SF network occurs. The nonswelling of the cryogel by volume is due to the cryoconcentration phenomenon producing a very high concentration of SF and PDMAA in the unfrozen domains of the cryogelation reactions forming the pore walls of the cryogel.[29]

The total porosity P and the pore volume V_p of the cryogel were measured as 93.7 ± 0.5% and 11.5 $mL{\cdot}g^{-1}$, respectively, indicating a highly porous structure with interconnected open

https://doi.org/10.1021/acsapm.2c00741
ACS Appl. Polym. Mater. 2022, 4, 5234−5245

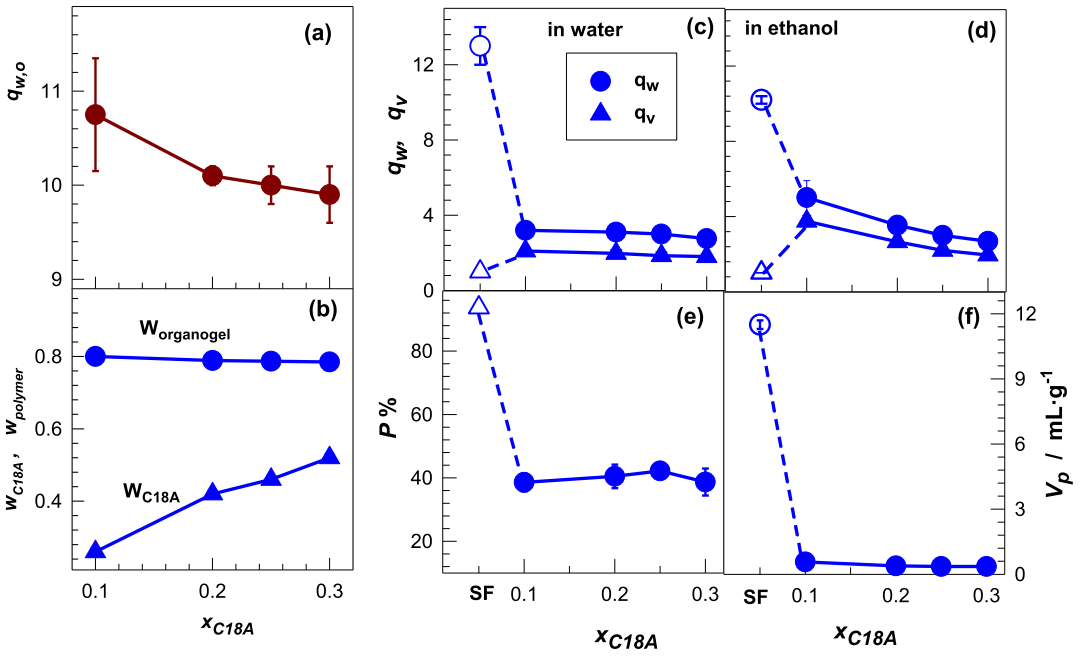

Figure 3. (a) Weight swelling ratio $q_{w,o}$ of the cryogel in the monomer solution, plotted against the mole fraction of C18A of the solution x_{C18A}. (b) Weight fractions of C18A units (w_{C18A}) and organogel ($w_{organogel}$) in the OHGs, shown as a function of x_{C18A}. (c,d) Weight (q_w) and volume swelling ratios (q_v) of OHGs in water (c) and ethanol (d), plotted against x_{C18A}. (e,f) Total porosity P (e) and pore volume V_p (f) shown as a function of x_{C18A}. Open symbols in (c–f) represent the data of the starting cryogel.

pores. Scanning electron microscopy (SEM) and confocal microscopy measurements indeed revealed a macroporous structure of the cryogel scaffold with interconnected pores (Figure 1c–e). The scaffold exhibits a honeycomb morphology consisting of quasi-spherical pores. The sphere-equivalent diameter of the pores varies between 23 and 73 μm, with an average diameter of 44 ± 12 μm (Figure 1f).

Figure 2a shows compressive stress–strain curves of the wet cryogel and the corresponding SF hydrogel formed at 50 °C.[40] The inset of the figure is a semi-logarithmic plot of the data to highlight the low-strain regime. Although both the cryogel and hydrogel sustain 96% compression, the wet cryogel exhibits a Young's modulus E of 90 ± 20 kPa and a fracture stress σ_f of 6.1 ± 0.8 MPa, which are around 15 and 8 times higher than those of the hydrogel (6.1 ± 0.5 kPa and 0.8 ± 0.2 MPa, respectively). Moreover, the stress–strain curve of the cryogel exhibits a plateau-like regime below 60% strain, during which the stress only slightly increases with increasing strain (inset of Figure 2a). We can explain this regime with the deformation of the pore walls under strain during which water in the cryogel is forced out of the pores so that the cryogel easily deforms. Moreover, the steep increase of the stress–strain curve above 60% strain is attributed to the compression of the nearly nonporous cryogel network with completely squeezed pore walls.

This explanation was indeed observed visually, as shown in Figure 2b. Here, a cryogel specimen in the wet state is compressed up to 80% and then unloaded to zero strain. Because the weight swelling ratio q_w of the cryogel is 13 ± 1, the water content of the specimen is around 92 wt %, the rest being the SF/PDMAA network forming the pore walls. It is seen that this large amount of water in the cryogel is forced out of the pores due to its incompressibility during compression. Interestingly, during unloading, water expelled from the pores is absorbed again, and the sample recovers its original shape within seconds without damage. In contrast to the cryogel, the hydrogel underwent an irreversible (permanent) deformation until it fractures at 95 ± 2% compression. The observed behavior of the cryogel associated with the flowing-out and flowing-in water through the pores due to the elastic pore walls is known as poroelasticity and is also observed in soft tissues, such as articular cartilage, providing their biomechanical functions including load bearing ability.[47−49] The reversible flowing-out and flowing-in water through the pores of the cryogels were also demonstrated by rheological tests, as detailed in the Supporting Information text and Figure S5. Concluding this section, the mechanically robust SF cryogel component of OHGs presented here not only exhibits a high porosity and a macroporous structure with interconnected μm-sized pores, but also its pore walls are elastic withstanding large deformations without a permanent damage. These extraordinary material properties are due to the cryoconcentration phenomenon occurring at the beginning of the cryogelation reactions.[28,29,34] Thus, during freezing of the reaction system at −18 °C, the reactants are expelled from the ice crystals and accumulate in the unfrozen domains to form a highly concentrated solution where the reaction occurs. As a consequence, these unfrozen domains forming the pore walls of the cryogel consist of a high concentration SF and PDMAA, exhibiting elasticity and mechanical strength.

2.2. Formation of OHGs. The OHGs were prepared in two steps, namely, (i) immersing freeze-dried cryogel specimens in an ethanolic solution of AAc and C18A monomers, *N*,*N*′-methylenebis(acrylamide) (BAAm) cross-linker, and α,α′-azoisobutyronitrile (AIBN) initiator and (ii) free radical copolymerization reactions at 50 °C within the pores of the cryogel. The total monomer concentration (C_o) in the ethanolic solution was fixed at 41 w/v % throughout this study, while the mole fraction of C18A, denoted by x_{C18A}, was varied between 0.10 and 0.30. The concentrations of BAAm and AIBN were 1 mol % with respect to the monomers. Similar

https://doi.org/10.1021/acsapm.2c00741
ACS Appl. Polym. Mater. 2022, 4, 5234−5245

to the swelling behavior of the cryogel in water, the cryogel volume in the monomer solution remained unchanged, while its weight significantly increased due to the filling of the pores with the solution. The weight swelling ratio of the cryogels in the monomer solution, denoted by $q_{w,o}$, slightly decreased from 11 to 10 with increasing C18A content of the solution (Figure 3a).

After immersing the cryogel specimens in the reaction solution for 10 min, the solution containing cryogels were transferred into several plastic syringes, and free radical copolymerization reactions were conducted at 50 °C for 24 h. In this way, SF scaffolds containing poly(AAc-*co*-C18A) organogel in their pores were obtained. They were then immersed in ethanol to extract soluble species for one week by replacing it every second day and then immersed in water to reach swelling equilibrium. The gel fraction W_g was found to be 0.96 ± 0.02 for the OHG formed at x_{C18A} = 0.10, while at higher C18A contents, all the monomers were completely incorporated into the pores of the cryogel scaffold. The weight fractions of C18A units and poly(AAc-*co*-C18A) organogel in OHGs with respect to dry states, represented by w_{C18A} and $w_{organogel}$, respectively, were calculated as

$$w_{C18A} = w_{organogel} m_{C18A} \quad (1)$$

$$w_{organogel} = \frac{(q_{w,o} - 1)\, C_o}{1 + (q_{w,o} - 1) C_o} \quad (2)$$

where m_{C18A} is the weight fraction of C18A in the monomer mixture. As seen in Figure 3b, the weight fraction of C18A (w_{C18A}) in OHGs increases from 26 to 52% as x_{C18A} is increased from 0.10 to 0.30, while the organogel weight fraction remains almost constant at 79%. The high amount of the organogel introduced in the scaffold is due to its large pore volume acting as the reaction loci for the formation of microinclusions.

Figure 3c,d shows the weight (q_w) and volume swelling ratios (q_v) of OHGs in water (c) and ethanol (d). For comparison, the data of the starting cryogel scaffold are also shown by the open symbols. As compared to the scaffold, the weight swelling ratio q_w of OHGs in water significantly decreases, while their volume swelling ratio q_v slightly increases. The increase in q_v is attributed to the hydrophilicity of AAc units of the organogel in the OHG, while decreasing q_w reflects decreasing porosity. Because ethanol is a better solvent for poly(AAc-*co*-C18A) as compared to SF,[50] OHGs attain higher volumes and masses when immersed in ethanol. Figure 3e,f compares the total porosity P (e) and the pore volume V_p (f) of the starting scaffold (open symbols) with OHGs (filled symbols). Both P and V_p decrease from 93.7 ± 0.5 to 40 ± 2% and from 11.5 to 0.36−0.57 mL·g^{-1}%, respectively, after incorporation of the organogel in the pores of the cryogel scaffold reflecting pore filling with the organogel component.

Figure 4 shows SEM images of the starting scaffold (left) and the OHG prepared at x_{C18A} = 0.30 (right). The honeycomb pore morphology of the scaffold can also be seen after incorporation of the organogel in the pores. Indeed, the size distribution of the pores estimated from the images remained unchanged at 44 ± 12 μm. However, a closer examination of the SEM images reveals that as compared to the scaffold, the deepness of the pore holes disappears in the OHG, as shown in the zoomed-in images in the bottom panel of Figure 4. Similar SEM images were also obtained for OHGs

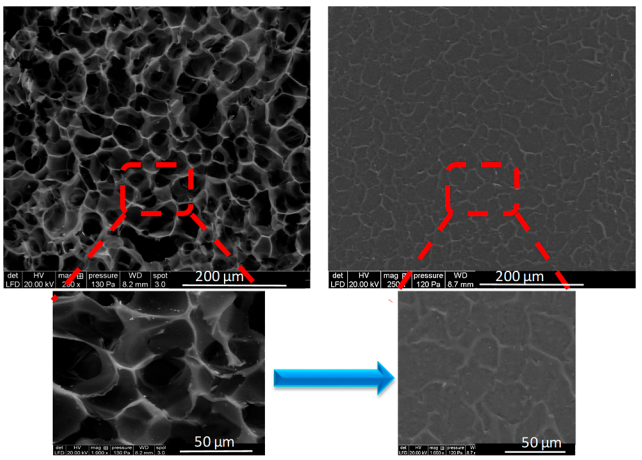

Figure 4. SEM images of the starting cryogel (left) and the OHG prepared at x_{C18A} = 0.30 (right). The images in the bottom panel are zoomed in to the indicated areas.

prepared at various x_{C18A} between 0.10 and 0.30 (Figure S6). Increasing C18A content of the monomer solution decreased the deepness of the pore holes, as revealed by the decrease of the white area fraction in the images, while the pore diameters remained constant (Figures S6 and S7). To visualize the distribution of the organogel and scaffold components in the OHGs, confocal microscopy measurements were conducted on an OHG specimen formed at x_{C18A} = 0.30 after staining its organogel and scaffold components red and green, respectively. Figures 5a−c and S8a−c show confocal microscopy images of the scaffold (a) and organogel phases (b), and the OHG (c). Some black areas are seen in Figure 5c, indicating the existence of the unfilled pores in the OHG. Moreover, although the combination of the green scaffold and red organogel should predominantly result in a yellow color for the OHG, it appears yellowish orange, revealing the presence of an excess amount of the organogel component in the OHG. Nevertheless, the images reflect that the organogel component distributes over the whole scaffold to produce an OHG consisting of the SF scaffold with μm-sized pores partially filled with poly(AAc-*co*-C18A) organogel.

2.3. Thermal, Viscoelastic, and Mechanical Properties of OHGs. Figure 6a shows differential scanning calorimetry (DSC) thermograms of the starting cryogel and OHGs prepared at various x_{C18A}, as indicated. As expected, no peak appears in the thermogram of the SF cryogel, while OHGs exhibit a melting peak that becomes sharper and shifts to a higher temperature with increasing C18A content. The melting temperature T_m of OHG slightly increases from 49 ± 1 to 54 ± 1 °C as x_{C18A} is increased from 0.10 to 0.30. Upon cooling from above to below T_m, no crystallization peak appeared in the DSC scan for OHG with x_{C18A} = 0.10, which is attributed to the steric hindrance of the cryogel scaffold to the reformation of crystalline domains (Figure S9). For OHGs with a higher x_{C18A}, the crystallization temperature T_{cry} increases from 40 ± 1 to 43 ± 1 °C with increasing x_{C18A}. Figure 6b shows the degree of crystallinity f_{cry} of OHGs, which is the fraction of C18A units forming side chain crystals, plotted against x_{C18A}. f_{cry} increases from 0.013 ± 0.001 to 0.13 ± 0.01 with increasing x_{C18A} from 0.10 to 0.30, indicating that 1.3 to 13% of C18A units in the pores of the scaffold form crystalline domains. The f_{cry} values are much smaller than those reported for semicrystalline hydrogels based on AAc and C18A

https://doi.org/10.1021/acsapm.2c00741
ACS Appl. Polym. Mater. 2022, 4, 5234−5245

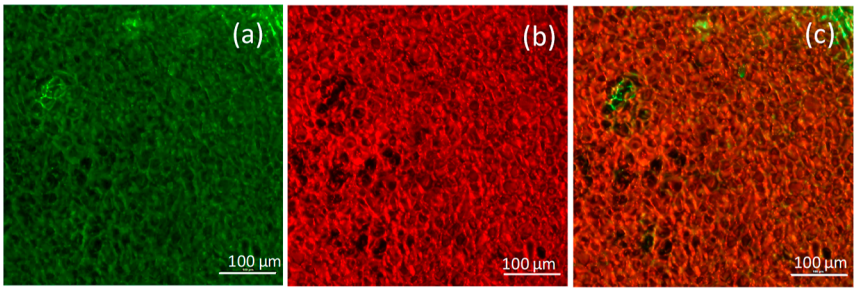

Figure 5. Confocal microscopy images of the OHG formed at x_{C18A} = 0.30. The cryogel scaffold was stained green using FITC, while poly(AAc-*co*-C18A) micro-inclusion was stained with Nile red. The images show the SF scaffold (a) and organogel phases (b), and the OHG (c).

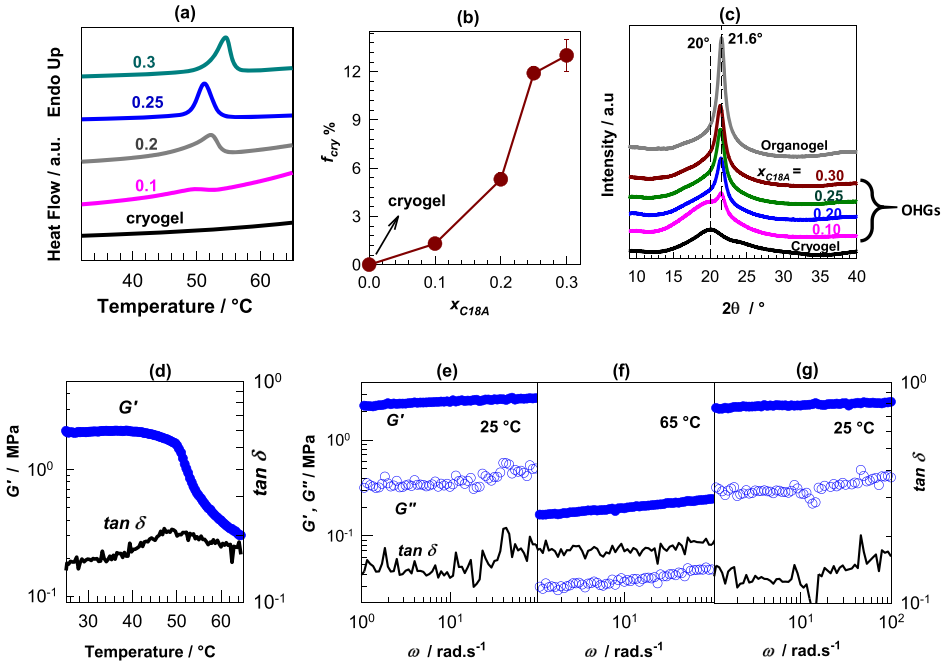

Figure 6. (a) DSC scans of the cryogel scaffold and OHGs formed at various x_{C18A} indicated. (b) Degree of crystallinity f_{cry} plotted against x_{C18A}. (c) XRD scans of SF cryogel, OHGs, and the poly(AAc-*co*-C18A) organogel with x_{C18A} = 0.30. (d) Temperature dependence of G' (symbols) and tan δ (lines) for an OHG formed at x_{C18A} = 0.30. The specimen is heated from 25 to 65 °C at a rate of 4 °C·min^{-1}. ω = 6.3 rad·s^{-1}. γ_o = 0.1%. (e–g) Frequency (ω) sweep results of an OHG specimen at 25 (e) and 65 °C (f), and after cooling back to 25 °C (g). G', G'', and tan δ are shown by the filled and open symbols, and lines, respectively. x_{C18A} = 0.30. γ_o = 0.1%.

(10–35%),[51,52] which is attributed to the confinement of the poly(AAc-*co*-C18A) organogel within the pores of OHG, limiting the alignment of C18 side chains.

Figure 6c shows XRD patterns of OHGs at various x_{C18A} together with their components, namely, SF cryogel and poly(AAc-*co*-C18A) organogel with x_{C18A} = 0.30. In accordance with the DSC results, XRD patterns of OHGs and organogel exhibit a distinct peak at 21.6°, corresponding to a *d*-spacing of 0.41 nm, that is, the distance between two aligned C18 side chains perpendicular to the same polymer backbone.[52,53] This peak becomes sharper as x_{C18A} is increased, reflecting increasing degree of crystallinity. Moreover, the broad peak at 20° that appears in the cryogel and becomes a shoulder to the main peak of OHG with x_{C18A} = 0.10 is typical for PDMAA existing in the cryogel network.[54]

The crystallinity created in OHGs provided them switchable mechanics and viscoelasticity in response to a change in the temperature between below and above T_m. Figure 6d shows the variations of the storage modulus G' and loss factor tan δ (= G''/G' where G'' is the loss modulus) of an OHG specimen formed at x_{C18A} = 0.30 during heating from 25 to 65 °C at a rate of 4 °C·min^{-1}. The storage modulus G' decreases sevenfold (from 2 to 0.3 MPa) upon heating above T_m, while tan δ remains above 0.1, as typical for a so-called weak hydrogel.[55] Because tan δ represents the ratio of the dissipated energy to the stored energy under the sinusoidal deformation, this reveals that the melting of C18 crystals in OHG decreases the solid-like character of OHG, while its dissipative properties remain almost preserved. Figure 6e–g shows G', G'' , and tan δ of the same OHG at 25 (e) and 65 °C (f), and after cooling back to 25 °C (g), as a function of the angular frequency ω. G' exhibits a power law increase with ω, $G' \sim \omega^n$ at both below and above T_m, with the exponent n slightly increasing by heating above T_m from 0.036 ± 0.006 to 0.089 ± 0.001, indicating the more viscous character of the OHG above T_m as compared to that below T_m. Moreover, cooling the OHG specimen from 65 to 25 °C recovers both its initial modulus G′ and the exponent n of the frequency dependence. This shows that OHGs have reversibly switchable viscoelasticity in response to a change in the temperature between below and above T_m.

https://doi.org/10.1021/acsapm.2c00741
ACS Appl. Polym. Mater. 2022, 4, 5234–5245

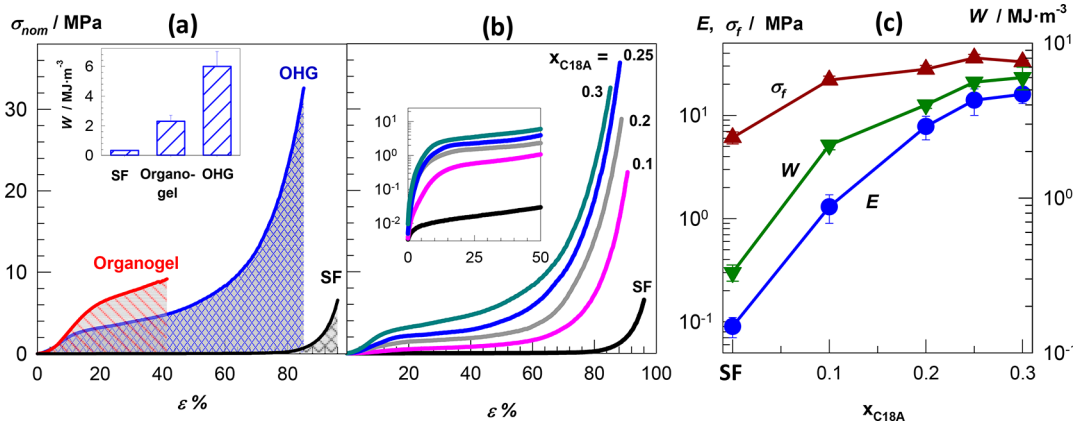

Figure 7. (a) Compressive stress−strain curves of the OHG with x_{C18A} = 0.30, and its organogel and SF cryogel components. The shaded area represents the energy to break (toughness) the gels. The inset shows the toughness W of the OHG and its components. (b) Compressive stress−strain curves of OHGs with various x_{C18A} and its SF cryogel component. The inset represents a semi-logarithmic plot of the same data up to 50% strain to highlight the low-strain regime. (c) Young's modulus E, fracture stress σ_f, and toughness W of OHGs and the SF cryogel shown as a function of x_{C18A}.

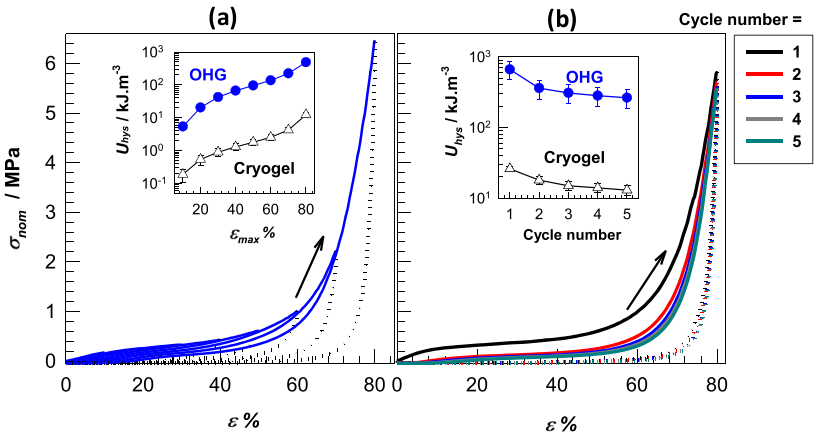

Figure 8. Successive loading and unloading cycles of OHG specimens with x_{C18A} = 0.10. (a) Eight successive cycles with increasing ε_{max} from 10 to 80%. (b) Five successive cycles up to a fixed ε_{max} of 80%. Loading and unloading curves are shown by the solid and dotted curves. The insets show the hysteresis energy U_{hys} for the OHG (filled symbols) and the cryogel (open symbols) plotted against ε_{max} (a) and the cycle number (b).

The mechanical performances of OHGs were determined by uniaxial compression tests at 23 ± 2 °C. Figure 7a compares the stress−strain curve of the OHG formed at x_{C18A} = 0.30 with its poly(AAc-*co*-C18A) organogel and SF cryogel components, where the shaded areas under the curves represent their toughness W, that is, the energy to break. The toughness W of the OHG is 6 ± 1 MJ·m^{-3}, which is 3- and 18-fold higher than that of the organogel and cryogel components, respectively (2.3 ± 0.4 and 0.33 ± 0.04 MJ·m^{-3}), reflecting that the combination of the OHG components in a single gel results in a significant toughness improvement (inset of Figure 7a). Figure 7b,c presents stress−strain curves of OHGs formed at various x_{C18A} and the starting SF cryogel and their mechanical parameters. The inset of (b) represents a semi-logarithmic plot of the same data up to 50% strain. A significant enhancement in all mechanical properties is observable after incorporation of the organogel component into the pores of the cryogel scaffold. For instance, the modulus E of the cryogel increases from 90 ± 20 kPa to 16 ± 3 MPa at x_{C18A} = 0.30, indicating 180-fold increase in its stiffness. Increasing C18A content of the organogel also increases the modulus, fractures stress, and toughness, while deformation at break slightly decreases but still remains above 85%. This increase is attributed to the C18A units forming alkyl crystals in μm-sized pores of the cryogel. Moreover, the increase in the plateau stress of OHGs with increasing x_{C18A} also reflects increasing stability of their pores filled with the organogels (inset of Figure 7b). We should note that the compressive mechanical properties of OHGs are much higher than those of the cryogels[29,34,35,37−39] and OHGs reported before.[7−10,14−16,18,19,21]

The dramatic increase in the mechanical strength of OHGs as compared to the cryogel and organogel components and their toughening mechanism are attributed to the significant energy dissipation in OHG networks. Thus, the brittle organogel component of the OHG in the dispersed phase acts as a sacrificial bond and fractures at a low strain, 40% (Figure 7a), by dissipating energy, while the continuous SF scaffold phase keeps the OHG together. This mechanism is similar to that of double-network hydrogels composed of tough and ductile components.[56,57] To verify the toughening mechanism of OHGs, successive loading−unloading cycles were conducted up to a maximum compressive strain ε_{max} of 80% with a waiting time of 5 min between cycles.

Figure 8a,b shows eight successive cycles with increasing ε_{max} from 10 to 80% (a) and five successive cycles up to a fixed

https://doi.org/10.1021/acsapm.2c00741
ACS Appl. Polym. Mater. 2022, 4, 5234−5245

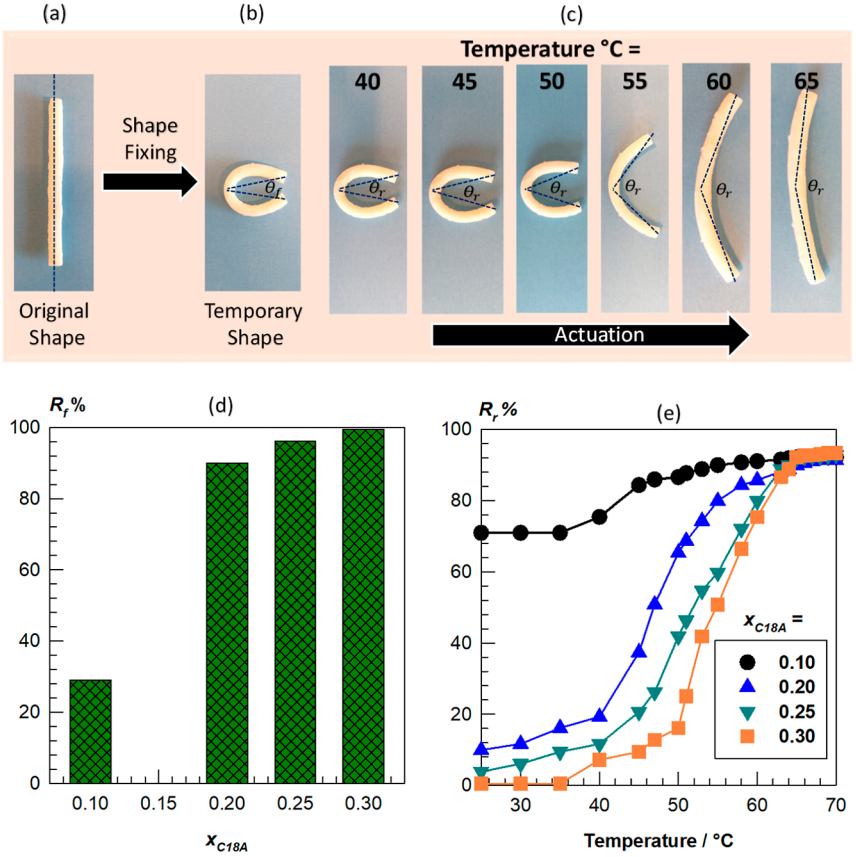

Figure 9. (a–c) Shape-fixity and shape-recovery behavior of an OHG specimen with x_{C18A} = 0.30. θ_f and θ_r are the fixed angle after unloading, and the recovered angle at the temperature indicated, respectively. (d,e) Shape-fixity ratio R_f (d) and the temperature-dependent recovery ratio R_r (e) for OHGs with various x_{C18A}.

ε_{max} of 80% (b), for OHG specimens with x_{C18A} = 0.10. The cyclic tests were also conducted on the cryogel component of the OHG under the same test conditions (Figure S10). The cyclic stress–strain curves of both OHG and cryogel show different paths of the loading and unloading curves, represented by the solid and dotted curves, respectively. The insets of Figure 8a,b shows the hysteresis energy U_{hys}, that is, the area covered by the loading and unloading curves, for the OHG (filled symbols) and the cryogel (open symbols) plotted against ε_{max} (a) and cycle number (b). It is seen that U_{hys} for OHG is an order of magnitude higher than that of the cryogel. Because U_{hys} is a measure of energy dissipation during a mechanical cycle, it reveals that a much larger amount of energy is dissipated from OHG as compared to the cryogel during each cycle. Assuming that the viscoelastic effect in stress–strain curves is negligibly small, the extra energy dissipation is due to the microscopic fracture of the organogel by dissipating energy before the catastrophic failure of the OHG structure. Thus, the toughening of the SF cryogel occurs due to the introduction of the brittle organogel component acting as sacrificial bonds and hence energy dissipative structure.

2.4. Shape-Memory Behavior of OHGs. All OHGs reported here exhibited shape-memory function induced by heating above the melting temperature T_m of their crystalline domains. For instance, the images in Figure 9a–c show the shape-fixity and shape-recovery behavior of an OHG specimen with x_{C18A} = 0.30. Its permanent shape is rod shape (a). Heating above T_m (65 °C), deforming to a horseshoe-like temporary shape, followed by cooling below T_m (25 °C), fixes its temporary shape (b). The specimen returns to its initial shape by increasing the temperature above T_m (c). The shape-memory behavior of OHGs is attributed to the coexistence of C18 crystals in the microinclusions and the cryogel matrix forming their skeleton. Thus, C18 crystals confined within the pores act as switching segments to fix the temporary shape, while the continuous cryogel component determines its permanent shape due to the entropic elasticity of the pore walls.

Figure 9d,e shows the shape fixity ratio R_f and the temperature dependent shape-recovery ratio R_r of OHGs, respectively, calculated as

$$R_f = \frac{\theta_f - 180}{\theta_d - 180} \quad (3)$$

$$R_r = \frac{\theta_d - \theta_r}{\theta_d - 180} \quad (4)$$

where θ_d, θ_f, and θ_r are the deformed angle under load, fixed angle after unloading, and recovered angle upon heating, respectively. Figure 9d reveals that the R_f ratio significantly increases with increasing x_{C18A} of OHGs, that is, with increasing degree of crystallinity. For instance, R_f increases from 29 to 99.5% with increasing x_{C18A}, indicating that the OHG at x_{C18A} = 0.30 is able to fix its temporary shape almost completely. Moreover, all OHGs exhibit a shape-recovery ratio R_r of more than 92% at 70 °C, reflecting their switchable mechanical properties in response to temperature (Figure 9e).

https://doi.org/10.1021/acsapm.2c00741
ACS Appl. Polym. Mater. 2022, 4, 5234–5245

3. CONCLUSIONS

Soft materials containing both hydrophilic and lyophilic phases, namely, OHGs, have great potential in various applications including sensors, microfluidics and optical devices, signal transmission, freeze-tolerant materials, and soft robotics. Here, we presented a facile strategy to obtain adaptive OHGs with tunable and programmable mechanics and viscoelasticity. We utilize the hydrophilic cryogel scaffold as the continuous phase, while the pores of the scaffold act as the reaction loci for the formation of microinclusions. Thus, the pores are filled with a monomer, crystallizable hydrophobic co-monomer, chemical cross-linker, and an initiator, and then, free-radical polymerization is conducted within the pores of the cryogel to fabricate OHGs containing hydrophobic microinclusions. In the first step of OHG preparation, mechanically robust cryogels based on meth-SF and PDMAA were prepared via cryogelation reactions at −18 °C. The cryogels with 94% porosity containing interconnected μm-sized pores were then immersed in an ethanolic solution of AAc, C18A, BAAm, and AIBN initiator. Polymerization reactions conducted within the pores of the cryogels lead to mechanically strong adaptive OHGs consisting of the SF scaffold containing semi-crystalline poly(AAc-*co*-C18A) organogel microinclusions.

A significant enhancement in all mechanical properties was observed after incorporation of the organogel component into the pores of the cryogel scaffold. The modulus E of the cryogel increases from 90 ± 20 kPa to 16 ± 3 MPa at x_{C18A} = 0.30, indicating 180-fold increase in its stiffness. Simultaneously, the fracture stress σ_f increases 5.4-fold (from 6.1 ± 0.8 to 33 ± 1 MPa), while the compression ratio at break remains almost constant. The dramatic increase in the mechanical strength of OHGs as compared to their components is attributed to the significant energy dissipation in OHG networks. Thus, the brittle organogel component in the pores, acting as a sacrificial bond, fractures at a low strain by dissipating energy, while the continuous SF scaffold phase keeps the OHG together. This toughening mechanism was also verified by successive loading−unloading cycles conducted up to a maximum compressive strain below failure. Increasing C18A content of the organogel also increases both the modulus and fracture stress, while deformation at break slightly decreases but still remains above 85%. This increase is attributed to the C18A units forming alkyl crystals in μm-sized pores of the cryogel. The melting temperature T_m and the degree of crystallinity of OHGs could be varied between 49 and 54 °C and 1.3−13%, respectively, by varying the amount of the crystallizable C18A units in the organogel component. The crystallinity created in OHGs provided them switchable mechanics and viscoelasticity, in response to a temperature change between below and above T_m. All OHGs exhibited shape-memory function with a shape-recovery ratio of more than 92%. Thus, OHGs presented here are a good candidate in various applications including biomedical, tissue engineering, aerospace, and electronics. The strategy developed here to obtain high-strength smart OHGs is suitable for a wide variety of combinations of hydrophilic scaffolds and organogels.

4. EXPERIMENTAL SECTION

4.1. Materials. *Bombyx mori* silkworm cocoons were obtained from Kozabirlik (Agriculture Sales Cooperative for Silk Cocoon, Bursa, Turkey). Lithium bromide (LiBr, Merck), sodium carbonate (Na_2CO_3, Merck), 1,4-BDDE (Sigma-Aldrich), TEMED, (Sigma-Aldrich), DMAA (Sigma-Aldrich, 99%), glycidyl methacrylate (GM, Sigma-Aldrich, 97%), APS (Sigma-Aldrich, ≥99%), *n*-octadecyl acrylate (C18A, Sigma-Aldrich, 97%), AIBN (Merck), *N*,*N*′-methylenebis(acrylamide) (BAAm, Sigma-Aldrich, 99%), ethanol (Merck, ≥99.9%), and polyethylene glycol (PEG-10000, Sigma-Aldrich, 10,000 g·mol^{-1}) were used without further purification. AAc (Merck) was used after filtering through an Al_2O_3 column to remove the hydroquinone inhibitor. FITC (Sigma-Aldrich, ≥90%) and Nile red (Sigma-Aldrich) were used for staining of the cryogel and the organogel parts of OHGs, respectively.

4.2. Isolation and Methacrylation of SF. The isolation and methacrylation of SF were performed as reported before.[40,58] Briefly, 10 g of *Bombyx mori* silkworm cocoons was cut into small pieces, and after cleaning with distilled water, they were boiled in an aqueous solution of Na_2CO_3 (1 L, 0.02 M) for 1 h to remove sericin proteins. After five-time washing of the SF with 1 L of distilled water at 70 °C for 20 min each, it was dried at room temperature for 2 days. 7 g of dried SF was then dissolved in 9.3 M LiBr solution (35 mL) at 60 °C within 2 h. After complete dissolution, 2 mL of GM was added for the methacrylation of SF, and stirring was continued at 60 °C for further 3 h at 500 rpm. This procedure resulted in meth-SF possessing a methacrylation degree of 14%, which was determined by ^{1}H-NMR as detailed in our previous work.[40] Finally, the solution was dialyzed using a dialysis tube (10,000 MWCO, Snake Skin, Pierce) against distilled water that was refreshed three times a day for 4 days. In this way, an aqueous solution of 7 w/v % meth-SF was obtained, as determined gravimetrically. In order to increase its concentration, meth-SF aqueous solution was further dialyzed against PEG-10000 solution (15 w/v %) using a dialysis tube of 3500 MWCO (Snake Skin, Pierce).

4.3. Fabrication of SF Cryogels and OHGs. The cryogels were prepared from an aqueous solution of meth-SF with a methacrylation degree of 14% and DMAA monomer as a spacer. BDDE was the cross-linker for SF while the APS-TEMED redox system was the initiator for DMAA. TEMED and APS concentrations were fixed at 0.025 v/v % and 3.51 mM, respectively,[40] while the BDDE concentration was decreased from 20 to 3 mmol·g^{-1} (with respect to meth-SF) with increasing amount of meth-SF to prevent early gelation of the reaction solution prior to the cryoconcentration of the reactants. The synthesis conditions were the same as those of the SF hydrogels we reported before,[40] except that the reaction temperature was reduced from 50 to −18 °C to provide cryogenic conditions. To optimize the formation conditions of SF cryogels, two series of experiments were carried out: in the first series, the concentration of meth-SF was fixed at 5 w/v %, while the DMAA content was varied from 0 to 10 w/v %. In the second series, the DMAA content was fixed at 2 w/v %, and the meth-SF concentration was changed between 5 and 15 w/v %. For instance, to fabricate a cryogel at meth-SF and DMAA concentrations of 5 and 2 w/v %, respectively, 0.200 g (0.208 mL) of DMAA and 1.00 mL of BDDE were first added to 7.14 mL of aqueous solution of 7.0 w/v % meth-SF. Then, 0.10 mL of APS and 0.125 mL of TEMED were introduced from their stock solutions into this mixture, whose amount was finally completed to 10 mL by using distilled water. Finally, homogeneous reaction solutions were transferred into several plastic syringes that were immediately placed at −18 °C for 24 h. After thawing, the cryogels were ejected from the syringes and placed in an excess of distilled water to remove the unreacted species. After 3 days, wet cryogels were dried using a freeze-dryer (Christ Alpha 2−4 LD-plus) by first freezing at −25 °C for 1 day, followed by freeze-drying at −40 °C/0.12 mbar vacuum and −60 °C/0.011 mbar vacuum for the second and the third day, respectively. For comparison, the corresponding hydrogels at meth-SF and DMAA concentrations of 5 and 2 w/v %, respectively, were also prepared at 50 °C for 24 h, as described previously.[40]

To fabricate OHGs, we used a cryogel scaffold prepared at meth-SF and DMAA concentrations of 5 and 2 w/v %, respectively. The cryogel specimens were immersed in ethanolic solutions containing AAc, C18A, AIBN, and BAAm at 40 °C. The total monomer (AAc + C18A) concentration was fixed at 41 w/v %, while the mole fraction of C18A, denoted by x_{C18A}, was varied between 0.10 and 0.30. The

https://doi.org/10.1021/acsapm.2c00741
ACS Appl. Polym. Mater. 2022, 4, 5234−5245

concentrations of the AIBN initiator and BAAm cross-linker were 1 mol % with respect to the total monomers. The cryogels immediately absorbed the solution to attain a constant mass. After 10 min, organic solution-embedded cryogel specimens were transferred into several plastic syringes together with the organic solution and placed in an oven at 50 °C to initiate the free radical copolymerization of AAc, C18A, and BAAm within the pores of the cryogels. After 24 h, OHGs were separated by peeling off the surrounding poly(AAc-*co*-C18A) organogel. The OHGs thus obtained were first placed in an excess of ethanol to remove unreacted species, and then in water at least for 1 week to replace ethanol. For comparison, poly(AAc-*co*-C18A) organogels with x_{C18A} = 0.30 were fabricated by the following route: AAc (1.32 mL) and C18A (2.70 g) were first dissolved in 4 mL ethanol at 40 °C. Then, AIBN and BAAm were added (both 1 mol % with respect to monomers) to this solution, and the final volume was completed to 10 mL with ethanol. Reaction solution was then transferred into several plastic syringes, and they were placed in an oven at 50 °C for 24 h. All material characterization studies were performed on the water-swollen OHGs, except XRD measurements where dry powdered OHG specimens were used.

4.4. Characterization of the Cryogels and OHGs. The weight (q_w) and volume (q_v) swelling ratios of the cryogels and OHGs were calculated using the equations $q_w = m/m_{dry}$ and $q_i = (D/D_{dry})^3$, respectively, where m and D are the weights and the diameters of the swollen specimens and m_{dry} and D_{dry} have the same meaning, but for their dry states. Gel fraction W_g showing the mass fraction of the reactants that incorporate into the water-insoluble gel was calculated as $W_g = m_{dry}/(m_0\ C)$, where m_0 is the mass of the as-prepared cryogel or OHG, and C is the total concentration of the reactants in the reaction solution.

To determine the conformation of SF in the cryogels, attenuated total reflection (ATR)−FTIR measurements were conducted on the Agilent Technologies Cary 630 ATR−FTIR spectrophotometer, as detailed before.[34−36] In short, the Amide-I region of the spectra was deconvolved by the Gaussian model after a linear baseline correction by using PeakFit software (Version 4.12, SeaSolve Software Inc). Then, the band positions at 1620, 1640, 1660, and 1698 cm^{-1}, corresponding to the β-sheet, random coil, α-helix, and β-turn respectively, were fixed for curve fitting, while allowing their widths and heights to vary (Figure S4a,b). DSC measurements were performed on the PerkinElmer DSC 4000 instrument under nitrogen atmosphere. Specimens of wet cryogels and OHGs of about 10 mg were put in aluminum pans, and then, they were scanned between 0 and 65 °C. Melting enthalpies ΔH_m were calculated from the DSC curves and the degree of crystallinity f_{cry}, that is, the fraction of C18A units forming crystalline regions was determined, as reported before.[53] XRD measurements were conducted on freeze-dried cryogels, OHGs, and poly(AAc-*co*-C18A) organogel on the PANalytical X-Pert PRO multi-purpose diffractometer using Ni-filtered Cu Kα (λ = 0.15418 nm) radiation at 45 kV and 40 mA in the range of 2θ = 5−40°.

To estimate the porosity of the cryogels and OHGs, we used their weight (q_w) and volume swelling ratios (q_v) in water. We should note that the q_w of cryogels includes water locating both in the gel and in the pores, while q_v is caused by the solvation of the cross-linked polymer chains, that is, pore walls. Thus, the total porosity, that is, the volume fraction of pores P of the cryogels and OHGs can be calculated from the difference between q_w and q_v using the equation[59]

$$P = 1 - q_v[1 + (q_w - 1)\rho/d_1]^{-1} \quad (5)$$

where d_1 and ρ are the densities of water (1.0 g·mL^{-1}) and SF scaffold (1.35 g·mL^{-1}) or OHG (1.1 g·mL^{-1}), respectively. Moreover, the total volume of the pores V_p was estimated from the mass increase of the scaffold and OHGs in water at pH = 3.0. It was found that in this solution, both the scaffold and OHGs do not swell by volume, that is, q_v = 1, so that the mass increase is related to the amount of the solvent within the pores. Thus, V_p was calculated as $V_p = {d_1}^{-1}(m/m_{dry} - 1)$.

SEM analysis was conducted on the FEI-QUANTA FEG 250 ESEM environmental electron microscope after coating the dry cryogels and the OHGs with platinum. To analyze the size distribution of the pores, randomly selected 50 pores from the SEM images were measured by using Image-Pro Plus 6 software, and their density distribution curves and the average sphere-equivalent pore diameters were determined.[53] To visualize the cryogel and the organogel components of the OHG, confocal laser scanning microscopy (CLSM, Nikon C2, Japan) was used after their staining with FITC and Nile Red, respectively.

Rheological measurements were conducted on a Bohlin Gemini 150 Rheometer system equipped with a Peltier device that controls the temperature. A parallel plate geometry (diameter = 20 mm) and a water trap were used. Frequency (ω) sweep tests on OHGs were conducted at both 25 and 65 °C at a fixed strain amplitude γ_o of 0.1%. Temperature-dependent viscoelastic properties of OHGs were determined by heating the OHG specimens from 25 to 65 °C at a fixed rate of 4 °C·min^{-1} at ω = 6.28 rad·s^{-1} and γ_o = 0.1%.

Mechanical performances of the cryogels and OHGs were determined at 23 ± 2 °C and at a test speed of 5 mm·min^{-1} by unidirectional compression tests performed using the Zwick-Roell universal test machine equipped with a load cell of 500 N. Young's modulus E was determined from the stress−strain curves between 2 and 4% compression. The stress was represented by its nominal value σ_{nom} (the force per cross-sectional area of the undeformed specimen), while strain was given by ε (sample length change relative to its initial length). The fracture stress and fracture strain were calculated from the maxima of the corresponding true stress−strain curves as detailed before.[60] Fatigue resistance of the cryogels and OHGs was determined via successive cyclic tests at the same test speed with a waiting time of 5 min between the cycles. The specimens were subjected to five successive loading−unloading cycles up to a maximum strain ε_{max} of 80%. In addition, step-wise cyclic tests were also conducted by increasing ε_{max} from 10 to 80% in eight steps.

Shape-memory tests were performed on the OHGs via bending tests. Straight cylindrical OHG specimens (5 cm in length, 4.3 mm in diameter) were heated up to 65 °C and deformed at this temperature to a horseshoe-like temporary shape with a deformed angle θ_d. They were then exposed to 25 °C for 5 min to fix this temporary shape under load. After unloading, fixed angles θ_f of the specimens were measured to determine the shape-fixity ratios R_f of OHGs. Finally, OHG specimens were gradually heated from 25 to 70 °C, recovery angles θ_r in each 1−3 °C temperature intervals were recorded, and shape-recovery ratios R_r were calculated.

■ ASSOCIATED CONTENT

Supporting Information

The Supporting Information is available free of charge at https://pubs.acs.org/doi/10.1021/acsapm.2c00741.

Details on the cryogel properties, cyclic strain-sweep tests, FTIR, DSC, SEM data, and cyclic mechanical test results (PDF)

■ AUTHOR INFORMATION

Corresponding Author

Oguz Okay − *Department of Chemistry, Istanbul Technical University, 34469 Istanbul, Turkey;* orcid.org/0000-0003-2717-4150; Phone: +90 212 285 3156; Email: okayo@itu.edu.tr

Author

Berkant Yetiskin − *Department of Chemistry, Istanbul Technical University, 34469 Istanbul, Turkey;* orcid.org/0000-0002-8696-6548

Complete contact information is available at: https://pubs.acs.org/10.1021/acsapm.2c00741

Author Contributions

The manuscript was written through contributions of all authors. All authors have given approval to the final version of the manuscript.

Funding

This work was supported by the Scientific and Technical Research Council of Turkey (TUBITAK) 1001, project no 121Z568. O.O. thanks the Turkish Academy of Sciences (TUBA) for the partial support.

Notes

The authors declare no competing financial interest.

REFERENCES

(1) Huang, J.; Fang, R.; Zhao, T.; Liu, M. Bioinspired Functional Organohydrogels with Synergistic Multiphases Heterostructure. *Polymer* **2020**, *190*, 122214.

(2) Mo, J.; Prévost, S. F.; Blowes, L. M.; Egertová, M.; Terrill, N. J.; Wang, W.; Elphick, M. R.; Gupta, H. S. Interfibrillar Stiffening of Echinoderm Mutable Collagenous Tissue Demonstrated at the Nanoscale. *Proc. Natl. Acad. Sci. U.S.A.* **2016**, *113*, E6362−E6371.

(3) Yang, Y.; Liu, Q.; Zhao, T.; Ru, Y.; Fang, R.; Xu, Y.; Huang, J.; Liu, M. Magnetic-Programmable Organohydrogels with Reconfigurable Network for Mechanical Homeostasis. *Nano Res.* **2021**, *14*, 255−259.

(4) Zhang, Z.; Hao, J. Bioinspired Organohydrogels with Heterostructures: Fabrications, Performances, and Applications. *Adv. Colloid Interface Sci.* **2021**, *292*, 102408.

(5) Storey, K. B.; Storey, J. M. Molecular Biology of Freezing Tolerance. *Compr. Physiol.* **2013**, *3*, 1283−1308.

(6) Xu, Y.; Rong, Q.; Zhao, T.; Liu, M. Anti-Freezing Multiphase Gel Materials: Bioinspired Design Strategies and Applications. *Giant* **2020**, *2*, 100014.

(7) Wu, J.; Wu, Z.; Xu, H.; Wu, Q.; Liu, C.; Yang, B.-R.; Gui, X.; Xie, X.; Tao, K.; Shen, Y.; Miao, J.; Norford, L. K. An Intrinsically Stretchable Humidity Sensor Based on Anti-Drying, Self-Healing and Transparent Organohydrogels. *Mater. Horiz.* **2019**, *6*, 595−603.

(8) Zhou, H.; Lai, J.; Zheng, B.; Jin, X.; Zhao, G.; Liu, H.; Chen, W.; Ma, A.; Li, X.; Wu, Y. From Glutinous-Rice-Inspired Adhesive Organohydrogels to Flexible Electronic Devices Toward Wearable Sensing, Power Supply, and Energy Storage. *Adv. Funct. Mater.* **2021**, *32*, 2108423.

(9) Jiang, L.; Liu, J.; He, S.; Liu, A.; Zhang, J.; Xu, H.; Shao, W. Flexible Wearable Sensors Based on Lignin Doped Organohydrogels with Multi-Functionalities. *Chem. Eng. J.* **2022**, *430*, 132653.

(10) Yu, Q.; Qin, Z.; Ji, F.; Chen, S.; Luo, S.; Yao, M.; Wu, X.; Liu, W.; Sun, X.; Zhang, H.; Zhao, Y.; Yao, F.; Li, J. Low-Temperature Tolerant Strain Sensors Based on Triple Crosslinked Organohydrogels with Ultrastretchability. *Chem. Eng. J.* **2021**, *404*, 126559.

(11) Wu, J.; Wu, Z.; Lu, X.; Han, S.; Yang, B.-R.; Gui, X.; Tao, K.; Miao, J.; Liu, C. Ultrastretchable and Stable Strain Sensors Based on Antifreezing and Self-Healing Ionic Organohydrogels for Human Motion Monitoring. *ACS Appl. Mater. Interfaces* **2019**, *11*, 9405−9414.

(12) Wu, J.; Wu, Z.; Wei, Y.; Ding, H.; Huang, W.; Gui, X.; Shi, W.; Shen, Y.; Tao, K.; Xie, X. Ultrasensitive and Stretchable Temperature Sensors Based on Thermally Stable and Self-Healing Organohydrogels. *ACS Appl. Mater. Interfaces* **2020**, *12*, 19069−19079.

(13) Zhao, Z.; Li, C.; Dong, Z.; Yang, Y.; Zhang, L.; Zhuo, S.; Zhou, X.; Xu, Y.; Jiang, L.; Liu, M. Adaptive Superamphiphilic Organohydrogels with Reconfigurable Surface Topography for Programming Unidirectional Liquid Transport. *Adv. Funct. Mater.* **2019**, *29*, 1807858.

(14) Zhang, Z.; Guo, L.; Zhang, X.; Hao, J. Environmentally Stable, Photochromic and Thermotropic Organohydrogels for Low Cost On-Demand Optical Devices. *J. Colloid Interface Sci.* **2020**, *578*, 315−325.

(15) Yang, Y.; Guan, L.; Li, X.; Gao, Z.; Ren, X.; Gao, G. Conductive Organohydrogels with Ultrastretchability, Antifreezing, Self-Healing, and Adhesive Properties for Motion Detection and Signal Transmission. *ACS Appl. Mater. Interfaces* **2018**, *11*, 3428−3437.

(16) Rong, Q.; Lei, W.; Chen, L.; Yin, Y.; Zhou, J.; Liu, M. Anti-Freezing, Conductive Self-Healing Organohydrogels with Stable Strain-Sensitivity at Subzero Temperatures. *Angew. Chem., Int. Ed.* **2017**, *56*, 14159−14163.

(17) Chen, F.; Zhou, D.; Wang, J.; Li, T.; Zhou, X.; Gan, T.; Handschuh-Wang, S.; Zhou, X. Rational Fabrication of Anti-Freezing, Non-Drying Tough Organohydrogels by One-Pot Solvent Displacement. *Angew. Chem., Int. Ed.* **2018**, *57*, 6568−6571.

(18) Liu, H.; Zhao, W.; Gao, G.; Ren, X. Tough, Anti-Freezing and Non-Drying Double Network Organohydrogels. *Mater. Today Commun.* **2019**, *21*, 100609.

(19) Zhuo, S.; Zhao, Z.; Xie, Z.; Hao, Y.; Xu, Y.; Zhao, T.; Li, H.; Knubben, E. M.; Wen, L.; Jiang, L.; Liu, M. Complex Multiphase Organohydrogels with Programmable Mechanics Toward Adaptive Soft-Matter Machines. *Sci. Adv.* **2020**, *6*, No. eaax1464.

(20) Ding, Q.; Wu, Z.; Tao, K.; Wei, Y.; Wang, W.; Yang, B.-R.; Xie, X.; Wu, J. Environment Tolerant, Adaptable and Stretchable Organohydrogels: Preparation, Optimization, and Applications. *Mater. Horiz.* **2022**, *9*, 1356−1386.

(21) Zhao, Z.; Zhang, K.; Liu, Y.; Zhou, J.; Liu, M. Highly Stretchable, Shape Memory Organohydrogels Using Phase-Transition Microinclusions. *Adv. Mater.* **2017**, *29*, 1701695.

(22) Sagiri, S. S.; Singh, V. K.; Kulanthaivel, S.; Banerjee, I.; Basak, P.; Battachrya, M. K.; Pal, K. Stearate Organogel−Gelatin Hydrogel Based Bigels: Physicochemical, Thermal, Mechanical Characterizations and In Vitro Drug Delivery Applications. *J. Mech. Behav. Biomed. Mater.* **2015**, *43*, 1−17.

(23) Gao, H.; Zhao, Z.; Cai, Y.; Zhou, J.; Hua, W.; Chen, L.; Wang, L.; Zhang, J.; Han, D.; Liu, M.; Jiang, L. Adaptive and Freeze-Tolerant Heteronetwork Organohydrogels with Enhanced Mechanical Stability Over a Wide Temperature Range. *Nat. Commun.* **2017**, *8*, 15911.

(24) Creton, C. 50th Anniversary Perspective: Networks and Gels: Soft but Dynamic and Tough. *Macromolecules* **2017**, *50*, 8297−8316.

(25) *Self-Healing and Self-Recovering Hydrogels*; Creton, C., Okay, O., Eds. ; Springer Nature. 2020, pp 1-379.

(26) Lozinsky, V. Cryostructuring of Polymeric Systems. 50. Cryogels and Cryotropic Gel-Formation: Terms and Definitions. *Gels* **2018**, *4*, 77.

(27) Lozinsky, V. I. Cryogels on the Basis of Natural and Synthetic Polymers: Preparation, Properties and Application. *Russ. Chem. Rev.* **2002**, *71*, 489−511.

(28) Lozinsky, V. I.; Okay, O. Basic Principles of Cryotropic Gelation. *Adv. Polym. Sci.* **2014**, *263*, 49−101.

(29) Okay, O.; Lozinsky, V. I. Synthesis and Structure−Property Relationships of Cryogels. *Adv. Polym. Sci.* **2014**, *263*, 103−157.

(30) Lozinsky, V. I.; Galaev, I. Y.; Plieva, F. M.; Savina, I. N.; Jungvid, H.; Mattiasson, B. Polymeric Cryogels as Promising Materials of Biotechnological Interest. *Trends Biotechnol.* **2003**, *21*, 445−451.

(31) Hixon, K. R.; Lu, T.; Sell, S. A. A Comprehensive Review of Cryogels and their Roles in Tissue Engineering Applications. *Acta Biomater.* **2017**, *62*, 29−41.

(32) Villard, P.; Rezaeeyazdi, M.; Colombani, T.; Joshi-Navare, K.; Rana, D.; Memic, A.; Bencherif, S. A. Autoclavable and Injectable Cryogels for Biomedical Applications. *Adv. Healthcare Mater.* **2019**, *8*, 1900679.

(33) Henderson, T. M. A.; Ladewig, K.; Haylock, D. N.; McLean, K. M.; O'Connor, A. J. Cryogels for Biomedical Applications. *J. Mater. Chem. B* **2013**, *1*, 2682−2695.

(34) Ak, F.; Oztoprak, Z.; Karakutuk, I.; Okay, O. Macroporous Silk Fibroin Cryogels. *Biomacromolecules* **2013**, *14*, 719−727.

(35) Yetiskin, B.; Akinci, C.; Okay, O. Cryogelation within Cryogels: Silk Fibroin Scaffolds with Single-, Double-and Triple-Network Structures. *Polymer* **2017**, *128*, 47−56.

(36) Yetiskin, B.; Okay, O. High-Strength and Self-Recoverable Silk Fibroin Cryogels with Anisotropic Swelling and Mechanical Properties. *Int. J. Biol. Macromol.* **2019**, *122*, 1279−1289.

(37) Shirbin, S. J.; Lam, S. J.; Chan, N. J.-A.; Ozmen, M. M.; Fu, Q.; O'Brien-Simpson, N.; Reynolds, E. C.; Qiao, G. G. Polypeptide-Based Macroporous Cryogels with Inherent Antimicrobial Properties: The Importance of a Macroporous Structure. *ACS Macro Lett.* **2016**, *5*, 552−557.
(38) Dai, R.; Meng, L.; Fu, Q.; Hao, S.; Yang, J. Fabrication of Anisotropic Silk Fibroin-Cellulose Nanocrystals Cryogels with Tunable Mechanical Properties, Rapid Swelling, and Structural Recoverability via a Directional-Freezing Strategy. *ACS Sustainable Chem. Eng.* **2021**, *9*, 12274−12285.
(39) Zhu, Y.; Liu, H.; Qin, S.; Yang, C.; Lv, Q.; Wang, Z.; Wang, L. Antibacterial Sericin Cryogels Promote Hemostasis by Facilitating the Activation of Coagulation Pathway and Platelets. *Adv. Healthcare Mater.* **2022**, *11*, 2102717.
(40) Oral, C. B.; Yetiskin, B.; Okay, O. Stretchable Silk Fibroin Hydrogels. *Int. J. Biol. Macromol.* **2020**, *161*, 1371−1380.
(41) de Queiroz, A. A. A.; Castro, S. C.; Higa, O. Z. Adsorption of Plasma Proteins to DMAA Hydrogels Obtained by Ionizing Radiation and its Relationship with Blood Compatibility. *J. Biomater. Sci. Polym. Edn.* **1997**, *8*, 335−347.
(42) Weng, L.; Gouldstone, A.; Wu, Y.; Chen, W. Mechanically Strong Double Network Photocrosslinked Hydrogels from N,N-Dimethylacrylamide and Glycidyl Methacrylated Hyaluronan. *Biomaterials* **2008**, *29*, 2153−2163.
(43) Babic, M.; Horak, D.; Jendelova, P.; Glogarova, K.; Herynek, V.; Trchova, M.; Likavcanova, K.; Lesny, P.; Pollert, E.; Hajek, M.; Sykova, E. Poly(N,N-dimethylacrylamide)-Coated Maghemite Nanoparticles for Stem Cell Labeling. *Bioconjugate Chem.* **2009**, *20*, 283−294.
(44) Chen, X.; Knight, D. P.; Shao, Z.; Vollrath, F. Conformation Transition in Silk Protein Films Monitored by Time-Resolved Fourier Transform Infrared Spectroscopy: Effect of Potassium Ions on Nephila Spidroin Films. *Biochemistry* **2002**, *41*, 14944−14950.
(45) Mo, C.; Holland, C.; Porter, D.; Shao, Z.; Vollrath, F. Concentration State Dependence of the Rheological and Structural Properties of Reconstituted Silk. *Biomacromolecules* **2009**, *10*, 2724−2728.
(46) Karakutuk, I.; Ak, F.; Okay, O. Diepoxide-Triggered Conformational Transition of Silk Fibroin: Formation of Hydrogels. *Biomacromolecules* **2012**, *13*, 1122−1128.
(47) Mow, V. C.; Kuei, S. C.; Lai, W. M.; Armstrong, C. G. Biphasic Creep and Stress Relaxation of Articular Cartilage in Compression: Theory and experiments. *J. Biomech. Eng.* **1980**, *102*, 73−84.
(48) Soltz, M. A.; Ateshian, G. A. Experimental Verification and Theoretical Prediction of Cartilage Interstitial Fluid Pressurization at an Impermeable Contact Interface in Confined Compression. *J. Biomech.* **1998**, *31*, 927−934.
(49) Malandrino, A.; Moeendarbary, E. Poroelasticity of Living Tissues. In *"Encyclopedia of Biomedical Engineering"*; Hellmich, C., Mantovani, D., Wong, A., Rymer, W. Z., Hargrove, L., Eds.; Elsevier: Amsterdam, 2019; Vol. 2, pp 238−245.
(50) Okay, O. Semicrystalline Physical Hydrogels with Shape-Memory and Self-Healing Properties. *J. Mater. Chem. B* **2019**, *7*, 1581−1596.
(51) Kurt, B.; Gulyuz, U.; Demir, D. D.; Okay, O. High-Strength Semi-Crystalline Hydrogels with Self-Healing and Shape Memory Functions. *Eur. Polym. J.* **2016**, *81*, 12−23.
(52) Bilici, C.; Can, V.; Nöchel, U.; Behl, M.; Lendlein, A.; Okay, O. Melt-Processable Shape-Memory Hydrogels with Self-Healing Ability of High Mechanical Strength. *Macromolecules* **2016**, *49*, 7442−7449.
(53) Su, E.; Bilici, C.; Bayazit, G.; Ide, S.; Okay, O. Solvent-Free UV Polymerization of n-Octadecyl Acrylate in Butyl Rubber: A Simple Way to Produce Tough and Smart Polymeric Materials at Ambient Temperature. *ACS Appl. Mater. Interfaces* **2021**, *13*, 21786−21799.
(54) Naohara, R.; Narita, K.; Ikeda-Fukazawa, T. Change in Hydrogen Bonding Structures of a Hydrogel with Dehydration. *Chem. Phys. Lett.* **2017**, *670*, 84−88.
(55) Ross-Murphy, S. B. Structure-Property Relationships in Food Biopolymer Gels and Solutions. *J. Rheol.* **1995**, *39*, 1451−1463.
(56) Gong, J. P. Why are Double Network Hydrogels So Tough? *Soft Matter* **2010**, *6*, 2583−2590.
(57) Cui, K.; Sun, T. L.; Liang, X.; Nakajima, K.; Ye, Y. N.; Chen, L.; Kurokawa, T.; Gong, J. P. Multiscale Energy Dissipation Mechanism in Tough and Self-Healing Hydrogels. *Phys. Rev. Lett.* **2018**, *121*, 185501.
(58) Kim, S. H.; Yeon, Y. K.; Lee, J. M.; Chao, J. R.; Lee, Y. J.; Seo, Y. B.; Sultan, M. T.; Lee, O. J.; Lee, J. S.; Yoon, S.-i.; Hong, I.-S.; Khang, G.; Lee, S. J.; Yoo, J. J.; Park, C. H. Precisely Printable and Biocompatible Silk Fibroin Bioink for Digital Light Processing 3D Printing. *Nat. Commun.* **2018**, *9*, 1620.
(59) Okay, O. Macroporous Copolymer Networks. *Prog. Polym. Sci.* **2000**, *25*, 711−779.
(60) Argun, A.; Can, V.; Altun, U.; Okay, O. Non-Ionic Double and Triple Network Hydrogels of High Mechanical Strength. *Macromolecules* **2014**, *47*, 6430−6440.

Recommended by ACS

Dual-Cross-linked Liquid Crystal Hydrogels with Controllable Viscoelasticity for Regulating Cell Behaviors
Shengyue Tang, Binghong Luo, *et al.*
MAY 03, 2022
ACS APPLIED MATERIALS & INTERFACES
READ

Dynamic Flexible Hydrogel Network with Biological Tissue-like Self-Protective Functions
Wenda Wang, Hongbo Zeng, *et al.*
DECEMBER 14, 2020
CHEMISTRY OF MATERIALS
READ

Anisotropic Hydrogels with High Mechanical Strength by Stretching-Induced Oriented Crystallization and Drying
Qiankun Sun, Feng Zhou, *et al.*
APRIL 22, 2020
ACS APPLIED POLYMER MATERIALS
READ

Injectable Lignin-co-Gelatin Cryogels with Antioxidant and Antibacterial Properties for Biomedical Applications
Tuerdimaimaiti Abudula, Adnan Memić, *et al.*
SEPTEMBER 13, 2021
BIOMACROMOLECULES
READ

Get More Suggestions >

https://doi.org/10.1021/acsapm.2c00741
ACS Appl. Polym. Mater. 2022, 4, 5234−5245